Bulk Scattering Properties for the Remote Sensing of Ice Clouds.

2: Narrowband Models

Bryan A. Baum[1], Ping Yang[2], Andrew J. Heymsfield[3],

Steven Platnick[4], Michael D. King[4], and Sarah M. Thomas[5]

[1] NASA Langley Research Center, Hampton, VA

[2] Texas A&M University, College Station, TX

[3] National Center for Atmospheric Research, Boulder, CO

[4] NASA Goddard Space Flight Center, Greenbelt, MD

[5] Cooperative Institute for Meteorological Satellite Studies, Madison, WI

For submission to the

Journal of Applied Meteorology

2004

Corresponding author: Dr. Bryan A. Baum, NASA LaRC, 1225 W. Dayton St., Madison, WI 53706. Phone: 608-263-3898; Fax: (608) 262-5974; E-mail: bryan.baum@ssec.wisc.edu

Abstract

This study examines the development of bulk single-scattering properties of ice clouds, including single-scattering albedo, asymmetry factor, and phase function, for a set of 1117 particle size distributions obtained from analysis of FIRE-I, FIRE-II, ARM-IOP, TRMM-KWAJEX, and CRYSTAL-FACE data. The primary focus is to develop band-averaged models appropriate for use by the MODIS imager on the EOS Terra and Aqua platforms, specifically for bands located at wavelengths of 0.65, 1.6, 2.1, and 3.75 μm. Our results indicate that there are substantial differences in the bulk scattering properties of ice clouds formed in areas of deep convection and those that exist in areas of much lower updraft velocities.

Band-averaged bulk scattering property results obtained from a particle-size dependent mixture of ice crystal habits are compared to those obtained assuming only solid hexagonal columns. The single-scatter albedo is lower for hexagonal columns than for a habit mixture for the 1.6, 2.1, and 3.75 μm bands, with the differences increasing with wavelength. In contrast, the asymmetry factors obtained from the habit mixture and only the solid hexagonal column are most different at 0.65 μm, with the differences decreasing as wavelength increases. At 3.75 μm, the asymmetry factor results from the two habit assumptions are almost indistinguishable. The asymmetry factor, single-scatter albedo, and scattering phase functions are also compared to the MODIS V1 models. Differences between the current and V1 models can be traced to the microphysical models, specifically the number of both the smallest and the largest particles assumed in the size distributions.

1. Introduction

The general approach for inferring ice cloud optical and microphysical properties from satellite imagery is to compare measured satellite radiances to radiative transfer (RT) calculations. The RT calculations account for viewing geometry, solar illumination, surface temperature, surface emissivity, surface albedo and bidirectional reflectance characteristics in addition to cloud macrophysical, microphysical, and optical properties. In this study, our goal is to demonstrate how ice cloud *in situ* measurements can be used to improve the range of bulk microphysical and optical properties in RT models. The focus in Part 1 of this study is on the cloud microphysical models, including the ice particle size and habit distributions. In this paper, the objective is to use the microphysical models to derive bulk optical properties. As a demonstration of the approach, bulk scattering properties are derived for 12 bands on the Moderate Resolution Imaging Spectroradiometer (MODIS).

The current operational MODIS cloud microphysical and optical retrievals are based on a set of 12 cirrus models developed for MODIS (Baum et al., 2000; King et al. 2004) and are referred to henceforth as Version 1, or V1. The cirrostratus (Cs) and cirrus uncinus distributions are described by Heymsfield (1975), while Heymsfield and Platt (1984) present two modified size distributions typical of warm and cold cirrus clouds and three additional cirrus distributions that represent midlatitude cirrus at $T = -20°C$, $T = -40°C$, and $T = -60°C$. The remaining models are from specific dates during the FIRE-I and FIRE-II field campaigns (FIRE refers to the First ISCCP Regional Experiment; ISCCP refers to the International Satellite Cloud Climatology Project). In the MODIS V1 models, the ice water content (IWC) ranges from 10^{-3} to 10^{-1} g m^{-3}. The 12 size distributions

cover a limited range of cloud microphysical properties and dynamical regimes, e.g., production in slowly ascending parcels with less than 100 cm s^{-1} updrafts. While the ice particle size distributions vary between the V1 models, the scattering property calculations are limited to five discrete particle size bins. When the maximum dimension D is small ($D < 70$ μm), i.e., for small ice crystals, the habits are prescribed as 50% bullet rosettes, 25% hexagonal plates, and 25% hollow columns. When $D > 70$ μm, the habit mixture is 30% aggregates, 30% bullet rosettes, 20% hexagonal plates, and 20% hollow columns. This mixture of habits is fixed for all 12 distributions in the Version 1 models.

In the present study our intent is to form a new set of ice cloud models based on the particle size distribution (PSD) and habit distribution observed by *in situ* measurements. The new ice cloud models represent a significant improvement in the treatment of both size distribution and particle habits. The new models are based on 45 size bins, and the percentage of crystal habits for each model is based on the analyses of Part 1.

Section 2 presents the scattering property libraries used in our analyses, while Section 3 outlines the development of the new models. Bulk scattering properties are provided in Section 4, while Section 5 summarizes and concludes our study.

2. Data

2.a. Moderate Resolution Imaging Spectroradiometer

The Moderate Resolution Imaging Spectroradiometer (MODIS) is a 36-channel whiskbroom scanning radiometer. The channels, known as bands in the MODIS terminology, span a range from 0.415 and 14.23 μm in four focal plane assemblies. Nadir spatial resolutions are 250 m (two bands at 0.65 and 0.86 μm), 500 m (five bands at 0.47, 0.56, 1.24, 1.63, and 2.13 μm), and 1000 m (29 bands). Each band's spectral response

function (SRF) is determined by an interference filter overlying a detector array that images a 10-km along-track swath for each scan, resulting in 40, 20, and 10 element arrays for the 250, 500, and 1000-m bands, respectively. MODIS has onboard calibration consisting of blackbodies for the IR bands, a solar diffuser panel for reflectance calibration up through the 2.1-μm MODIS band and an accompanying diffuser stability monitor for assessing the stability of the diffuser up to 1 μm. Two MODIS instruments are currently in orbit on the Earth Observing System (EOS) platforms, each at an altitude of 705 km. The Terra platform is in a descending orbit with an equatorial crossing of 1030 local time, while Aqua is in an ascending orbit with an equatorial crossing of 1330 local time.

2.b Ice Particle Scattering Properties

An extensive library of scattering properties has been developed for a set of ice particles that include droxtals, hexagonal plates, hollow columns, solid columns, three-dimensional bullet rosettes, and aggregates. The methods generally involve a combination of the improved geometric optics approach and the finite-difference time domain (FDTD) method (Yang and Liou, 1996a,b). Details regarding the development of scattering properties for solid columns are provided in Takano and Liou (1989), and for hollow columns and bullet rosettes in Yang et al. (2000). Yang and Liou (1998) describe the methodology for aggregates. Droxtals are described further in Yang et al. (2003) and Zhang et al. (2004).

The droxtal is used to represent the smallest particles in a size distribution, and have an aspect ratio approaching unity. Polycrystals include three-dimensional bullet rosettes and aggregates. Aggregates are composed of between 2 and 8 hexagonal columns that are attached together in a random fashion. The scattering property database has been de-

rived at 234 discrete wavelengths between 0.4 and 13 μm. Scattering properties have been computed for particles in 45 size bins spanning a maximum dimension range of 2 to 9500 μm. For droxtals, scattering properties have been calculated only for sizes up to 100 μm. Ice particle properties include volume V, projected area A, asymmetry factor g, scattering cross section σ_{sca}, extinction cross section σ_{ext}, the scattering phase function $P(\Theta)$, and the fraction of δ transmission energy f_δ, which is a contribution in the forward scattering direction due to the direct transmission of rays through two parallel particle-air interfaces. The δ transmission is significant for pristine ice crystals such as plates and columns at visible wavelengths, but decreases with increasing absorption (and hence wavelength).

3. Band-Averaged Bulk Scattering Properties

Table 1 lists the MODIS bands used in this study. The MODIS Version 1 models were built from ice crystal scattering calculations obtained at a central wavelength for each band. As in Nasiri et al. (2002), scattering calculations are performed at discrete wavelengths and then averaged over the spectral response function for each band. For MODIS solar bands ($\lambda < 3$ μm), the scattering properties at each wavelength within the band's response function are weighted additionally by the solar spectral irradiance $S(\lambda)$ (Kurucz et al. 1984; Neckel and Labs, 1984). For wavelengths longer than 3 μm, however, the solar spectrum $S(\lambda)$ is replaced with the Planck function $B(\lambda)$ that is representative of the thermal IR emission from an opaque ice cloud at 233 K.

The band-weighted mean scattering cross section is given by

$$\overline{\sigma}_{sca} = \frac{\int_{\lambda_1}^{\lambda_2}\int_{D_{min}}^{D_{max}}\left[\sum_{h=1}^{M}\sigma_{sca}(D,h,\lambda)f_h(D)\right]n(D)F_s(\lambda)S(\lambda)\,dDd\lambda}{\int_{\lambda_1}^{\lambda_2}\int_{D_{min}}^{D_{max}}\left[\sum_{h=1}^{M}f_h(D)\right]n(D)F_s(\lambda)S(\lambda)\,dDd\lambda}, \tag{1}$$

where $f_h(D)$ is the ice particle habit fraction for habit h, M is the number of habits, D is particle size, $n(D)$ is the particle density, λ is wavelength, $S(\lambda)$ is the spectral solar spectrum and $F_s(\lambda)$ is the spectral response function. The habit fraction is defined so that for each size bin,

$$\sum_{h=1}^{M}f_h(D)=1. \tag{2}$$

The band-weighted mean extinction cross section is given by:

$$\overline{\sigma}_{ext} = \frac{\int_{\lambda_1}^{\lambda_2}\int_{D_{min}}^{D_{max}}\left[\sum_{h=1}^{M}\sigma_{ext}(D,h,\lambda)f_h(D)\right]n(D)F_s(\lambda)S(\lambda)\,dDd\lambda}{\int_{\lambda_1}^{\lambda_2}\int_{D_{min}}^{D_{max}}\left[\sum_{h=1}^{M}f_h(D)\right]n(D)F_s(\lambda)S(\lambda)\,dDd\lambda}. \tag{3}$$

The single-scattering albedo $\overline{\omega}$ is determined by the ratio of the mean scattering and extinction cross sections:

$$\overline{\omega} = \frac{\overline{\sigma}_{sca}}{\overline{\sigma}_{ext}}. \tag{4}$$

Also of interest is the band-averaged scattering phase function

$$\overline{P}(\Theta) = \frac{\int_{\lambda_1}^{\lambda_2}\int_{D_{min}}^{D_{max}}\left[\sum_{h=1}^{M}P(\Theta,h,D,\lambda)\sigma_{sca}(D,h,\lambda)f_h(D)\right]n(D)F_s(\lambda)S(\lambda)\,dDd\lambda}{\int_{\lambda_1}^{\lambda_2}\int_{D_{min}}^{D_{max}}\left[\sum_{h=1}^{M}\sigma_{sca}(D,h,\lambda)f_h(D)\right]n(D)F_s(\lambda)S(\lambda)\,dDd\lambda}. \tag{5}$$

Note that the phase function is weighted by the scattering cross section in the integrand. The band-averaged asymmetry factor ($\overline{g}$) and fraction of δ transmission energy ($\overline{f}_\delta$) are also weighted by the scattering cross section:

$$\bar{g} = \frac{\int\limits_{\lambda 1}^{\lambda 2} \int\limits_{D\min}^{D\max} \left[\sum\limits_{h=1}^{M} g(h,D,\lambda)\sigma_{sca}(D,h,\lambda)f_h(D)\right] n(D)F_s(\lambda)S(\lambda)\,dDd\lambda}{\int\limits_{\lambda 1}^{\lambda 2} \int\limits_{D\min}^{D\max} \left[\sum\limits_{h=1}^{M} \sigma_{sca}(D,h,\lambda)f_h(D)\right] n(D)F_s(\lambda)S(\lambda)\,dDd\lambda}, \tag{6}$$

and

$$\bar{f}_\delta = \frac{\int\limits_{\lambda 1}^{\lambda 2} \int\limits_{D\min}^{D\max} \left[\sum\limits_{h=1}^{M} f\delta(h,D,\lambda)\sigma_{sca}(D,h,\lambda)f_h(D)\right] n(D)F_s(\lambda)S(\lambda)\,dDd\lambda}{\int\limits_{\lambda 1}^{\lambda 2} \int\limits_{D\min}^{D\max} \left[\sum\limits_{h=1}^{M} \sigma_{sca}(D,h,\lambda)f_h(D)\right] n(D)F_s(\lambda)S(\lambda)\,dDd\lambda}. \tag{7}$$

The fraction of δ transmission energy for the IR bands is essentially zero because absorption dominates scattering within the crystal.

4. **Results**

In this section we present the bulk scattering properties obtained for 1117 particle size distributions. The cloud temperatures for these size distribution data range from –25°C to –73°C. Results are presented as a function of both the effective diameter and median mass diameter. The bulk scattering properties will be presented as a comparison of two habit distributions: one involving only solid hexagonal crystals and the other involving a mixture of particle habits.

4.a Band averaged $\bar{g}$ and $\bar{\omega}$ values

Figure 1 shows band-averaged single-scatter albedo $\bar{\omega}$ derived using only solid hexagonal columnar particles, for MODIS bands 6 (1.64 μm), 7 (2.13 μm), and 20 (3.75 μm). At 1.64 μm, the values range from 0.96 for the lowest D_{eff}, to 0.84 for the distributions having the largest D_{eff}. The largest $\bar{\omega}$ values correspond to the CRYSTAL data, which have the lowest D_{eff} values and the coldest cloud temperatures as shown in Part 1.

It is interesting to note that the TRMM data seem to have slightly higher values of $\bar{\omega}$ than the FIRE-I, FIRE-II, ARM, and CRYSTAL-FACE campaigns. The same behavior is noted also for MODIS bands 7 and 20. The $\bar{\omega}$ values decrease for bands 7 and 20 compared to band 6 because of increasing ice absorption at the longer wavelengths.

Figure 2 shows the same analysis as for the previous figure but also superimposes the results obtained from a mixture of ice particle habits. Here, the results obtained from the use of only solid hexagonal columns are shown in gray, while the results from a particle habit mixture are shown in black. For MODIS bands 6, 7, and 20, $\bar{\omega}$ has higher values for a habit mixture for all but the lowest D_{eff} than for solid hexagonal columns only. For MODIS bands 6, 7, and 20, the differences are reduced between the TRMM data and other field campaign data.

The band-averaged asymmetry factor $\bar{g}$ is shown in Figure 3 for hexagonal columns only. The asymmetry factor tends towards smaller values at small D_{eff}, which is to be expected as light scattering becomes more isotropic for small particles. As D_{eff} increases past 100 μm, $\bar{g}$ tends to asymptote. The values of $\bar{g}$ for TRMM tend to be lower than for the other field campaigns, which reflect the characteristics primarily of the largest particles. Some of this difference may be mitigated given a more realistic habit to represent the largest crystals in a given size distribution.

Of real interest is the comparison of $\bar{g}$ between hexagonal columns and the ice habit mixture shown in Figure 4. The differences in MODIS bands 1, 6 and 7 are particularly striking. At 0.65 μm, the difference in $\bar{g}$ between columns and a habit mixture can be larger than 0.05, although the difference decreases as D_{eff} increases. For band 6 (1.64 μm), the asymmetry factor is higher by approximately 0.04 for D_{eff} sizes below 100 μm.

The offset is evident also for band 7. While less dramatic, the asymmetry factor tends to be higher for bands 20 and 31 for a habit mixture than for solid hexagonal columns alone. These results indicate that clouds modeled as a mixture of ice habits tend to be more forward scattering than clouds composed solely of hexagonal ice particles.

4.b Comparison of $\overline{g}$ and $\overline{\omega}$ with MODIS Version 1 models

How do the results of the previous section compare with the current set of MODIS V1 models? A comparison of $\overline{\omega}$ values is provided in Figure 5. The MODIS V1 values for the 12 models are superimposed as cyan diamond symbols over those for a habit mixture. There are two points to note about the single-scatter albedo comparison. With regard to D_{eff}, the range of values for MODIS V1 is much narrower than for the current results employing gamma size distributions. A given D_{eff} leads to similar values of $\overline{\omega}$ for both the MODIS V1 and gamma PSDs. One may also note that several of the MODIS V1 models have D_{eff} sizes that are smaller than any of those obtained from the use of the gamma PSDs. For these small D_{eff} values, the single-scatter albedo values are much higher than those of the gamma PSDs. However, the highest V1 $\overline{\omega}$ values tend to follow the monotonic relationship between D_{eff} and $\overline{\omega}$ noted previously.

Figure 6 shows the comparison of the MODIS V1 $\overline{g}$ values with those computed from the various PSDs derived from the field campaigns. At the shorter wavelengths (0.65 and 1.64 μm), the MODIS V1 models are significantly lower than the values computed for a habit mixture, but the differences narrow as wavelength (and hence absorption) increases. Part of the discrepancy might be explained by noting that the asymmetry factor tends to increase with particle size, especially at wavelengths with little absorption. Since more large particles are used in the PSDs due to our increased particle size discreti-

zation, and some habits have significantly increased values of asymmetry factor than others, the band-averaged asymmetry factor for our chosen habit mixture is generally higher the MODIS V1 models.

Based on our investigation, the issues with both $\bar{g}$ and $\bar{\omega}$ at small values of D_{eff} between the two sets of models can be explained through examination of the respective sets of PSDs. In Part I of this study, the first figure showed a sampling of the gamma PSDs. These size distributions are repeated in Figure 7 (in gray) along with the three MODIS V1 PSDs (in black) that have the smallest D_{eff} values. In these three V1 size distributions, there are roughly 1 to 2 orders of magnitude more particles in the 20-μm size bin than in the 50-μm size bin, and particle density drops off quickly as size increases. This strongly peaked PSD behavior is most similar to the CRYSTAL-FACE PSD, but even the CRYSTAL-FACE PSD does not have such a disparity in particle concentration over such a narrow size range. We note that earlier PSD spectra were derived in part from a combination of 2D-C/2D-P probe data in conjunction with the FSSP for small particles. There is now some question as to the reliability of the small particles counted by the FSSP, since large particles can break up upon entering the sampling volume, thereby elevating the number of small particles counted.

The primary issue seems to be one of determining the appropriate number of very small particles to use in a PSD. As a way to gain some sense of the sensitivity of small particles to D_{eff}, $\bar{g}$, and $\bar{\omega}$ calculations, we first note that the CRYSTAL-FACE PSDs tend to be the most narrow. This is to be expected as they were derived from the coldest cloud in our data set, and had the lowest IWC values. Thus the CRYSTAL-FACE PSDs are adopted for the sensitivity study and are modified as follows. The particle densities in

only the smallest size bins (< 20 µm) are multiplied by 100 in the first set of calculations, and by 1000 in the second set. By doing so, we will no longer be able to match closely with the *in situ* IWC values, but this is a simple experiment to gain some insight as to the sensitivity of the bulk scattering parameters to small particles.

Enhanced small particle results for $\bar{\omega}$ and $\bar{g}$ are shown in Figures 8 and 9. The results using the unmodified PSDs are shown in black or gray. The results obtained by multiplying the number of small particles by 100 (or 1000) are shown in green (or red). The cyan squares represent the MODIS V1 models. The MODIS V1 models provide similar $\bar{\omega}$ values as the current calculations, at least at wavelengths of 1.64 and 2.13 µm, but there are some differences at 3.75 µm over a small range in D_{eff} between 40 and 60 µm. For D_{eff} < 20 µm, the MODIS V1 $\bar{\omega}$ values overlay those obtained from the modified CRYSTAL-FACE PSDs.

The asymmetry factor seems to be more sensitive to the ice particle habit as shown in Figure 9. The MODIS V1 models $\bar{g}$ values do not exactly match those from the current set of PSDs, but this is probably due to the use of a different habit distribution. In these calculations, the comparison seems to hint at larger differences for D_{eff} > 80 µm. This is expected since the current results are based on integration of particle size over 45 size bins, where the V1 models employed only 5 size bins.

4.c Scattering Phase Functions

A discussion of the scattering phase functions follows in this section. To facilitate this discussion, the full set of phase functions for each MODIS band (derived following Eq. 5) is filtered and averaged as follows. The goal is to develop phase functions for a defined set of D_{eff}, which in this case is D_{eff} = 10 to 180 µm in increments of 10 µm, for a

total of 18 discrete D_{eff} values. We note that the only way to obtain phase functions, or any of the bulk scattering parameters for that matter, for D_{eff} at sizes less than 30 μm is to modify the PSDs as discussed in the previous section. The set of phase functions is augmented by the two sets of properties resulting from the modified CRYSTAL-FACE PSDs (i.e., one set in which the number of small particles is multiplied by 100, and the other by 1000).

The PSDs are averaged that fall within a narrow region around the target D_{eff} values; the width of the region is chosen such that between 10 and 20 individual PSDs can be averaged for each D_{eff}. For each D_{eff} value, a mean and standard deviation can be calculated for the phase function. Results for D_{eff} values of 20, 60, and 100 μm are shown in Figure 10 for the MODIS 1.64-μm band. The left hand column shows the phase function over the full 180° range in scattering angle Θ, while the right hand column shows the phase function over the forward peak in the scattering angle. At 20 μm, the largest variances occur at very small Θ of less than 2°. At $D_{eff} = 60$ and 100 μm, the largest variances occur near the minima at $\Theta = 20°$, 130°, and 170°.

A comparison with two of the MODIS V1 models is shown in Figure 11, again for the MODIS 1.64-μm band. The MODIS V1 cold cirrus (Cold Ci) model and the cirrus uncinus (Ci Uncinus) models (Baum et al. 2000) are chosen as they represent the extrema of the V1 models, having the smallest and largest D_{eff} values, respectively, of 13.4 and 117.8 μm. Note that the values provided in Baum et al. (2000) are a factor of 1.5 lower than the values provided here; this is a result of a slightly different definition of effective diameter in the earlier study. The averaged phase functions derived at D_{eff} of 10 and 100 μm are provided for comparison with the Cold Ci and Ci Uncinus V1 models. The upper

panel of Fig. 11 shows the full phase function, while the lower panel is of only the forward peak.

A comparison of the two small particle models (Cold Ci and $D_{eff} = 10$ μm) shows some interesting differences. The value of the phase function is higher for the V1 Cold Ci model than for the $D_{eff} = 10$ μm model both in the forward scattering direction ($1° < \Theta < 3°$) and at side scattering angles between 50° and 110°. However, for $4° < \Theta < 30°$, and at $\Theta > 120°$, the reverse is true. The primary difference between the two models is in the use of droxtals. Droxtals have some of the tendencies of spherical particles in that the side scattering is reduced in comparison to hexagonal columns, and backscattering is enhanced.

The two large particle models (Ci Uncinus and $D_{eff} = 100$ μm) match more closely than the small particle models. However, there are some regions where differences exist near the minima at $\Theta = 20°$, 40°, and 170°, and between $110° < \Theta < 140°$. The two models are quite similar in the magnitudes of the phase function in both the forward and backward peaks.

5. Summary

This study examines the development of bulk single-scattering properties, including single-scatter albedo, asymmetry factor, and phase function, for a set of 1117 particle size distributions. The primary focus is to develop band-averaged models appropriate for use by the MODIS imager on the EOS Terra and Aqua platforms, but the methodology can be applied easily to other imagers such as the Advanced Very High Resolution Radiometer (AVHRR) or the Along Track Scanning Radiometer (ATSR). The primary MODIS bands discussed in this study are located at wavelengths of 1.6, 2.1, and 3.75 μm.

These bands are chosen because of their use in inferring ice cloud optical thickness and effective particle size. The primary benefit derived from application of our methodology is that the microphysical attributes of each model, specifically median mass diameter and ice water content, are consistent with those obtained from the in situ measurements as discussed in Part 1. This aspect should help to facilitate comparisons of satellite-derived quantities with those obtained from ground-based or aircraft-based measurements.

The PSDs are derived from analysis of FIRE-I, FIRE-II, ARM-IOP, TRMM-KWAJEX, and CRYSTAL-FACE data. However, only the TRMM-KWAJEX data are obtained from tropical cirrus anvils. The PSDs for the TRMM data tend to follow exponential distributions rather than gamma distributions. For any given ice particle habit mixture, the bulk scattering properties of asymmetry factor and single-scatter albedo tend to fall into two groups, with one group containing the FIRE, ARM, and CRYSTAL-FACE data and the other group containing the TRMM data. We note that the CRYSTAL-FACE data are from an extremely cold, optically thin cirrus cloud near the tropopause rather than from an anvil associated with deep convection. The data seem to indicate that there are substantial differences between ice clouds formed in areas of deep convection and those that exist in areas of much lower updraft velocities.

Results obtained from a particle-size dependent mixture of ice crystal habits are compared to those obtained assuming only solid hexagonal columns. The single-scatter albedo is lower for hexagonal columns than for a habit mixture for the 1.6, 2.1, and 3.75 μm bands, with the differences increasing with wavelength. In contrast, the asymmetry factors obtained from the habit mixture and only the solid hexagonal columns are most different at 0.65 μm, with the differences becoming lower as wavelength increases. At

3.75 μm, the asymmetry factor results from the two habit assumptions are almost indistinguishable. The asymmetry factor is found to be sensitive to the largest particles and particle habits assumed in the size distributions.

Results for asymmetry factor and single-scatter albedo are also compared to the MODIS V1 models. The V1 models have values for effective diameter that are much smaller than those obtained from the 1117 PSDs. Further examination into this discrepancy showed that the number of small particles in the smallest size bin of the V1 models was 2 to 3 orders of magnitude higher than for the gamma distributions. As the number of small particles is unknown because of the difficulty in measuring them accurately, two additional sets of PSDs were obtained by modifying the CRYSTAL-FACE PSD set in the following fashion: one set was derived by multiplying the number of small particles in the gamma distribution (i.e., those particles having a maximum dimension of less than 20 μm) by a factor of 100; the other set by multiplying the small crystals by a factor of 1000. The CRYSTAL-FACE PSD set was chosen because it was sampled from the coldest cloud in the data set, and also had the lowest IWC values. Based on the "modified" CRYSTAL-FACE PSDs, the effective diameter was extended from a minimum of 30 μm to 10 μm. While arbitrary, this provides some insight as to the sensitivity of bulk scattering properties to the number of small particles.

Future research will be performed to assess further the difference between bulk scattering models obtained from ice clouds in convective versus non-convective regions. Also, we hope to revisit the small particle issue once more accurate measurements are available.

Acknowledgments

References

Baum, B. A., D. P. Kratz, P. Yang, S. Ou, Y. Hu, P. F. Soulen, and S. C. Tsay, 2000: Remote sensing of cloud properties using MODIS Airborne Simulator imagery during SUCCESS. I. Data and models. *J. Geophys. Res.*, **105**, 11767–11780.

Heymsfield, A. J., 1975: Cirrus uncinus generating cells and the evolution of cirroform clouds. Part I. Aircraft observations of the growth of the ice phase. *J. Atmos. Sci.*, **32**, 799–808.

Heymsfield, A. J., and C. M. R. Platt, 1984: A parameterization of the particle size spectrum of ice clouds in terms of the ambient temperature and the ice water content. *J. Atmos. Sci.*, **41**, 846–855.

Heymsfield, A. J., A. Bansemer, P. R. Field, S. L. Durden, J. Stith, J. E. Dye, W. Hall, and T. Grainger, 2002: Observations and parameterizations of particle size distributions in deep tropical cirrus and stratiform precipitating clouds: Results from in situ observations in TRMM field campaigns. *J. Atmos. Sci.*, **59**, 3457–3491.

King, M. D., S. Platnick, P. Yang, G. T. Arnold, M. A. Gray, J. C. Riédi, S. A. Ackerman, and K. N. Liou, 2004: Remote sensing of liquid water and ice cloud optical thickness and effective radius in the Arctic: Application of airborne multispectral MAS data. *J. Atmos. Oceanic Technol.*, **21**, 857–875.

Kurucz, R. L., I. Furenlid, J. Brault, and L. Testerman, 1984: Solar flux atlas from 296 to 1300 nm, in *National Solar Observatory Atlas No. 1*, 239 pp., Nat. Solar Obs., Sunspot, N. M.

Nasiri, S. L., B. A. Baum, A. J. Heymsfield, P. Yang, M. Poellot, D. P. Kratz, and Y. Hu, 2002: Development of midlatitude cirrus models for MODIS using FIRE-I, FIRE-II,

and ARM *in-situ* data. *J. Appl. Meteor.,* **41**, 197–217.

Neckel, H., and D. Labs, 1984: The solar radiation between 3300 and 12500 angstroms, *Sol. Phys*., 90, 205–258.

Takano, Y., and K. N. Liou, 1989: Radiative transfer in cirrus clouds. Part I: Single-scattering and optical properties of oriented hexagonal ice crystals. *J. Atmos. Sci*., **46**, 3–19.

Yang, P., and K. N. Liou, 1996a: Finite-difference time domain method for light scattering by small ice crystals in three-dimensional space, *J. Opt. Soc. Amer. A*., *13*, 2072–2085.

Yang, P., and K. N. Liou, 1996b: Geometric-optics-integral-equation method for light scattering by nonspherical ice crystals, *Appl. Opt*., *35*, 6568–6584.

Yang, P., K. N. Liou, K. Wyser, and D. Mitchel, 2000: Parameterization of the scattering and absorption properties of individual ice crystals. *J. Geophys. Res*., **105**, 4699-4718.

Yang, P., B. A. Baum, A. J. Heymsfield, Y. X. Hu, H. L. Huang, S. C. Tsay, and S. Ackerman, 2003: Single scattering properties of droxtals. *J. Quant. Spectrosc. Radiat. Transfer*, 79-80, 1159–1169.

Zhang, Z., P. Yang, G. W. Kattawar, S. C. Tsay, B. A. Baum, Y. X. Hu, A. J. Heymsfield, and J. Reichardt, 2004: Geometric optics solution for the scattering properties of droxtal ice crystals. *Appl. Opt*., **43**, 2490–2499.

List of Tables

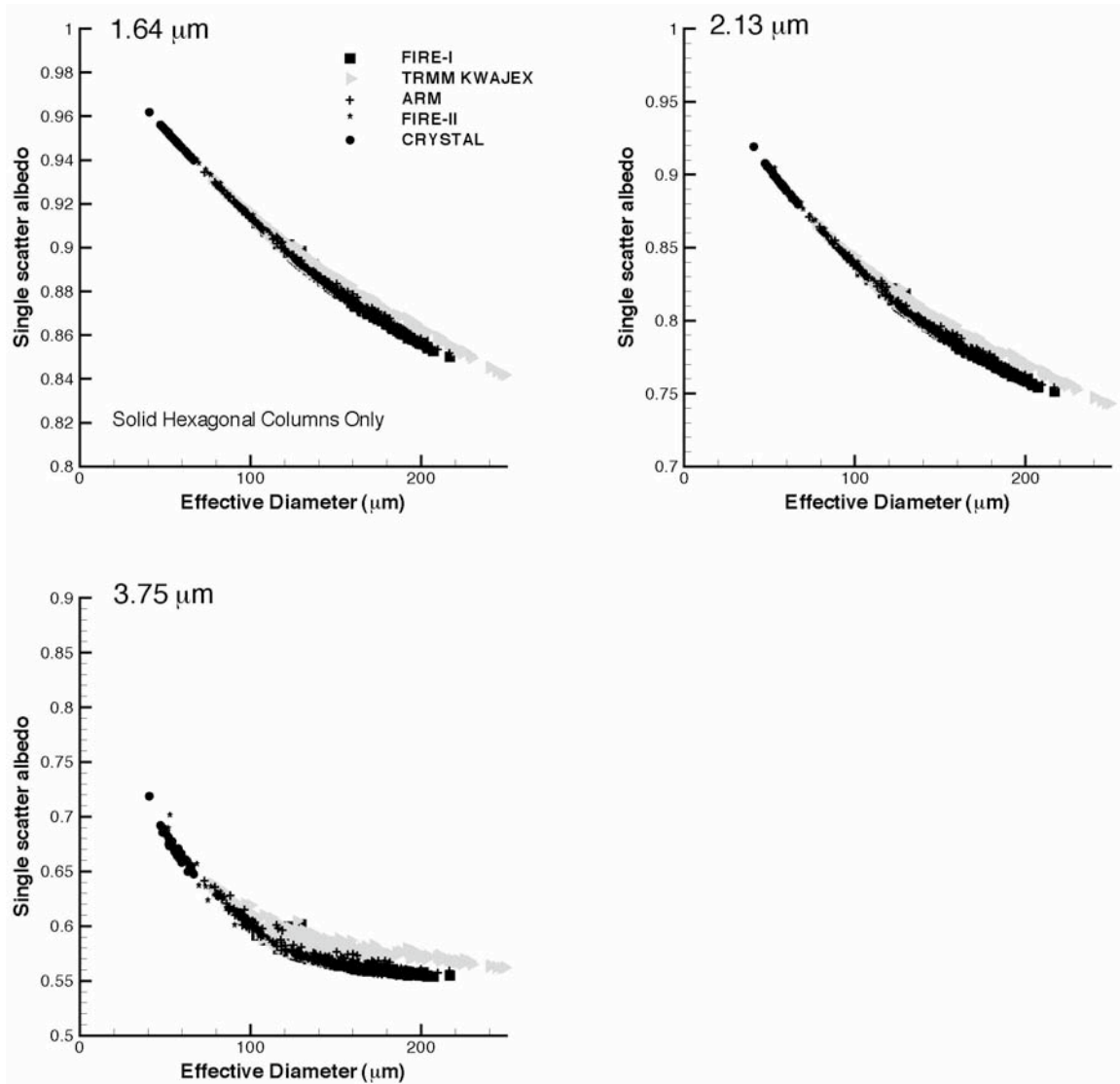| MODIS band	Wavelength range (μm)	Principal Absorbing Components
1	0.62-0.67	H_2O, O_3
6	1.628-1.652	H_2O, CO_2, CH_4
7	2.105-2.155	H_2O, CO_2, CH_4, N_2O
20	3.66-3.84	H_2O, CO_2, CH_4

List of figures

Figure 1: MODIS band-averaged single-scatter albedo calculated from *in situ* particle size distributions (PSDs) assuming a single ice particle habit of solid hexagonal columns. The PSD results from FIRE-I, FIRE-II, ARM, and CRYSTAL-FACE are black symbols; the results from the TRMM KWAJEX PSD data are denoted by gray symbols.

Figure 2: MODIS band-averaged single-scatter albedo calculated from *in situ* particle size distributions (PSDs) assuming a mixture of ice particle habits (black symbols), including droxtals, solid and hollow columns, plates, 3-D bullet rosettes and aggregates. Also shown are the results using the assumption of solid hexagonal columns only (gray symbols).

Figure 3: MODIS band-averaged asymmetry factor calculated from *in situ* particle size distributions (PSDs) assuming a single ice particle habit of solid hexagonal columns. The PSD results from FIRE-I, FIRE-II, ARM, and CRYSTAL-FACE are black symbols; the results from the TRMM KWAJEX PSD data are denoted by gray symbols.

Figure 4: MODIS band-averaged asymmetry factor calculated from *in situ* particle size distributions (PSDs) assuming a mixture of ice particle habits (black symbols), including droxtals, solid and hollow columns, plates, 3-D bullet rosettes and aggregates. Also shown are the results using the assumption of solid hexagonal columns only (gray symbols).

Figure 5: MODIS band-averaged single-scatter albedo calculated from *in situ* particle size distributions (PSDs) assuming a mixture of ice particle habits. The PSD results from FIRE-I, FIRE-II, ARM, and CRYSTAL-FACE are black symbols; the results from the TRMM KWAJEX PSD data are denoted by gray symbols. Superimposed on the data are the MODIS Version 1 (V1) models.

Figure 6: MODIS band-averaged asymmetry factor calculated from *in situ* particle size distributions (PSDs) assuming a mixture of ice particle habits. The PSD results from FIRE-I, FIRE-II, ARM, and CRYSTAL-FACE are black symbols; the results from the TRMM KWAJEX PSD data are denoted by gray symbols. Superimposed on the data are the MODIS Version 1 (V1) models.

Figure 7: As shown in Figure 1 in Part 1, five particle size distributions (gray lines) selected from the various field experiments. Superimposed over these PSDs are three PSDs from the MODIS Version 1 microphysical models used to generate the scattering models. These V1 models were chosen because they have the smallest effective diameters. The V1 models have at least one order of magnitude more small particles at 20 μm than at 50 μm.

Figure 8: MODIS band-averaged single-scatter albedo calculated from *in situ* particle size distributions (PSDs) assuming a mixture of ice particle habits. The PSD results from FIRE-I, FIRE-II, ARM, and CRYSTAL-FACE are black symbols; the results from the TRMM KWAJEX PSD data are denoted by gray symbols. Superimposed on the data are
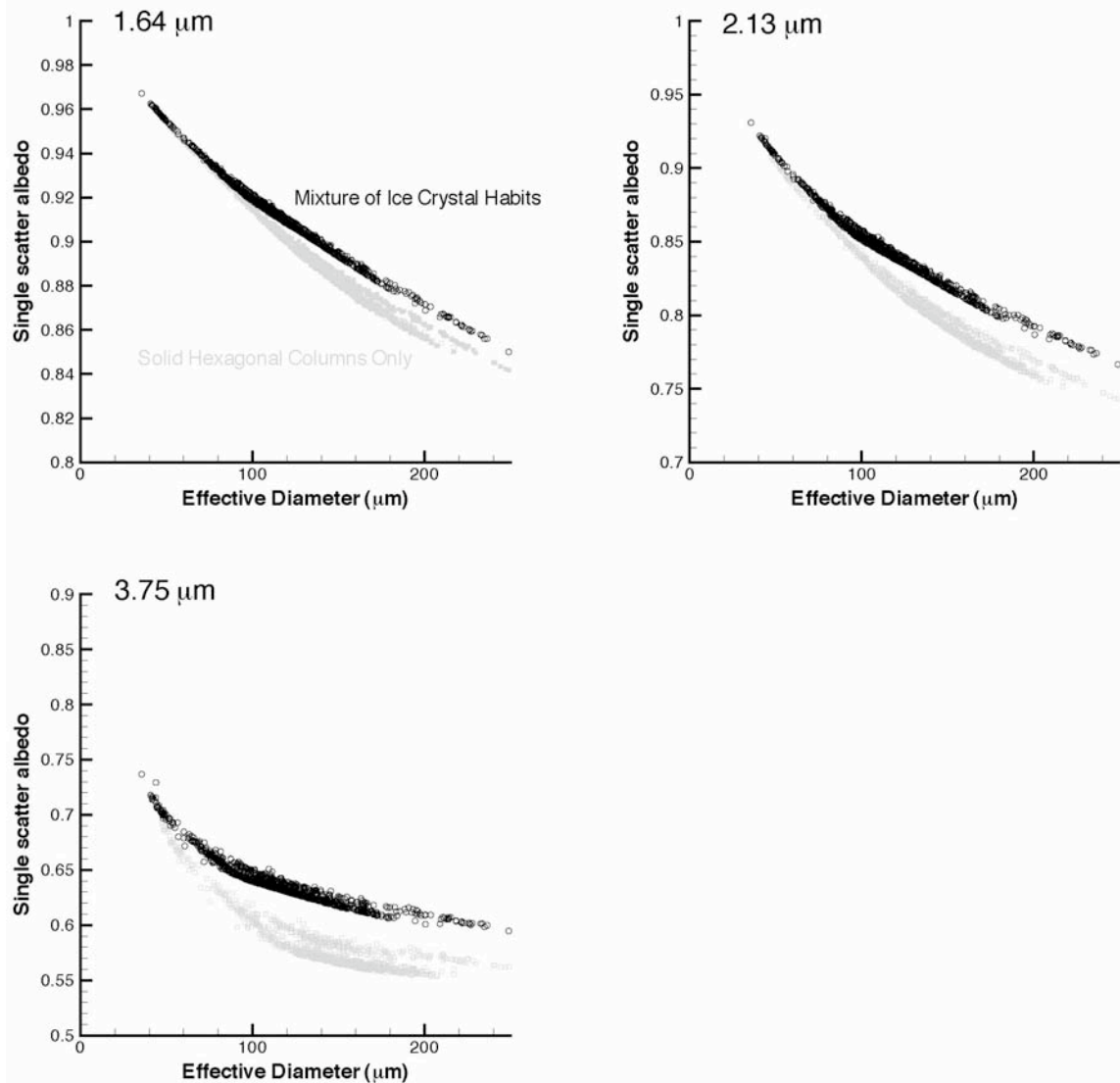
the results from a sensitivity study involving the CRYSTAL-FACE PSDs in which the number of particles with sizes less than 20 µm were multiplied by a factor of 100 (green symbols) or multiplied by a factor of 1000 (red symbols). The twelve MODIS V1 models are superimposed for reference (blue symbols).

Figure 9: Same as for Figure 8 but for MODIS band-averaged asymmetry factor.

Figure 10: For MODIS band 6 (1.64 µm), the scattering phase function mean (solid line) and standard deviation (dotted line) for D_{eff} values of 20, 60, and 100 µm. The full phase function is shown in the left hand column, while the forward peak in the phase function is shown in the right hand column.

Figure 11: For MODIS band 6 (1.64 µm), comparison of two MODIS V1 models (Cold Ci, D_{eff} = 13.4 µm and Ci Uncinus, D_{eff} = 117.8 µm) with two new models at D_{eff} = 10 and 100 µm.
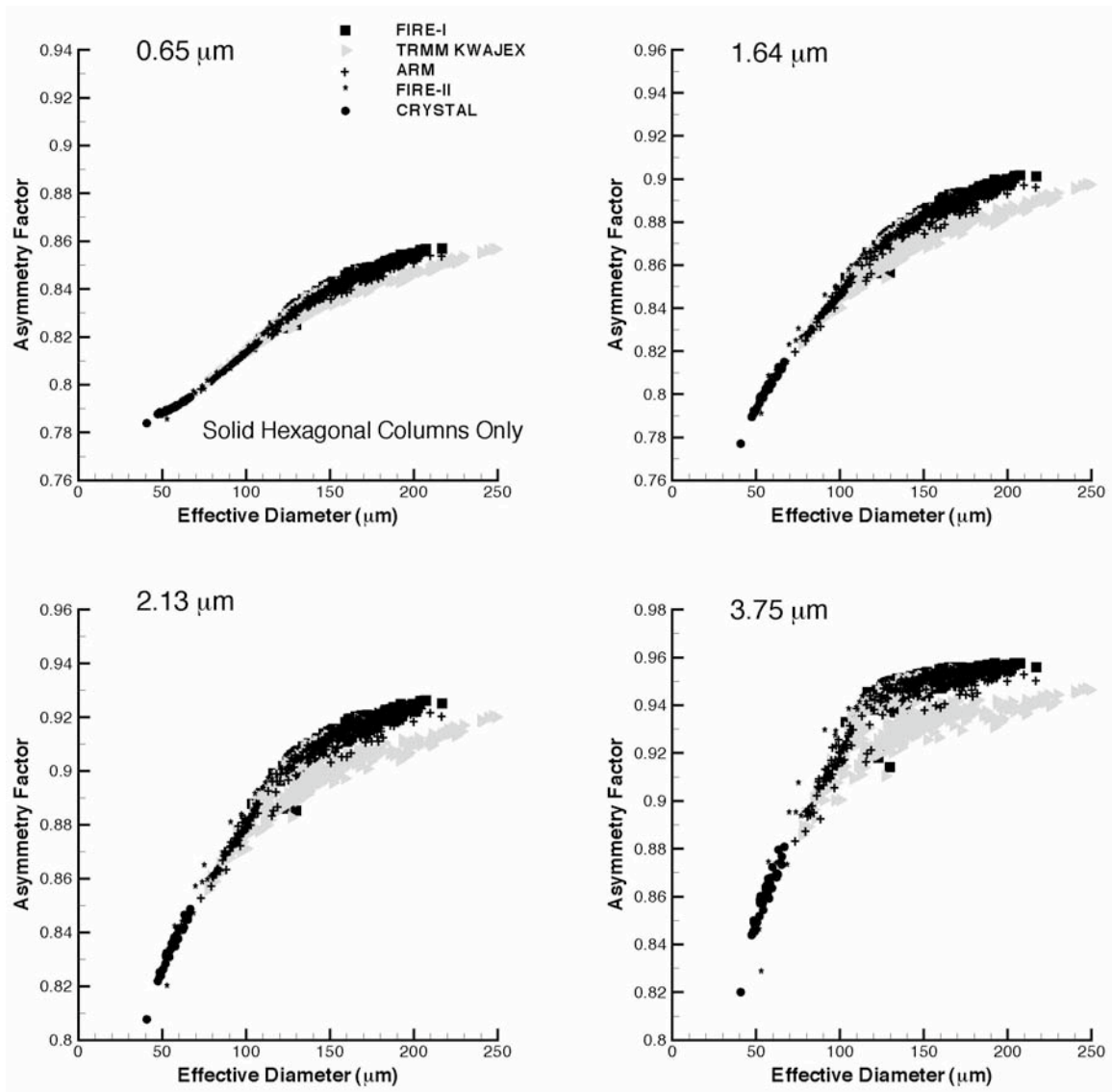
Figure 1. MODIS band-averaged single-scatter albedo calculated from *in situ* particle size distributions (PSDs) assuming a single ice particle habit of solid hexagonal columns. The PSD results from FIRE-I, FIRE-II, ARM, and CRYSTAL-FACE are black symbols; the results from the TRMM KWAJEX PSD data are denoted by gray symbols.
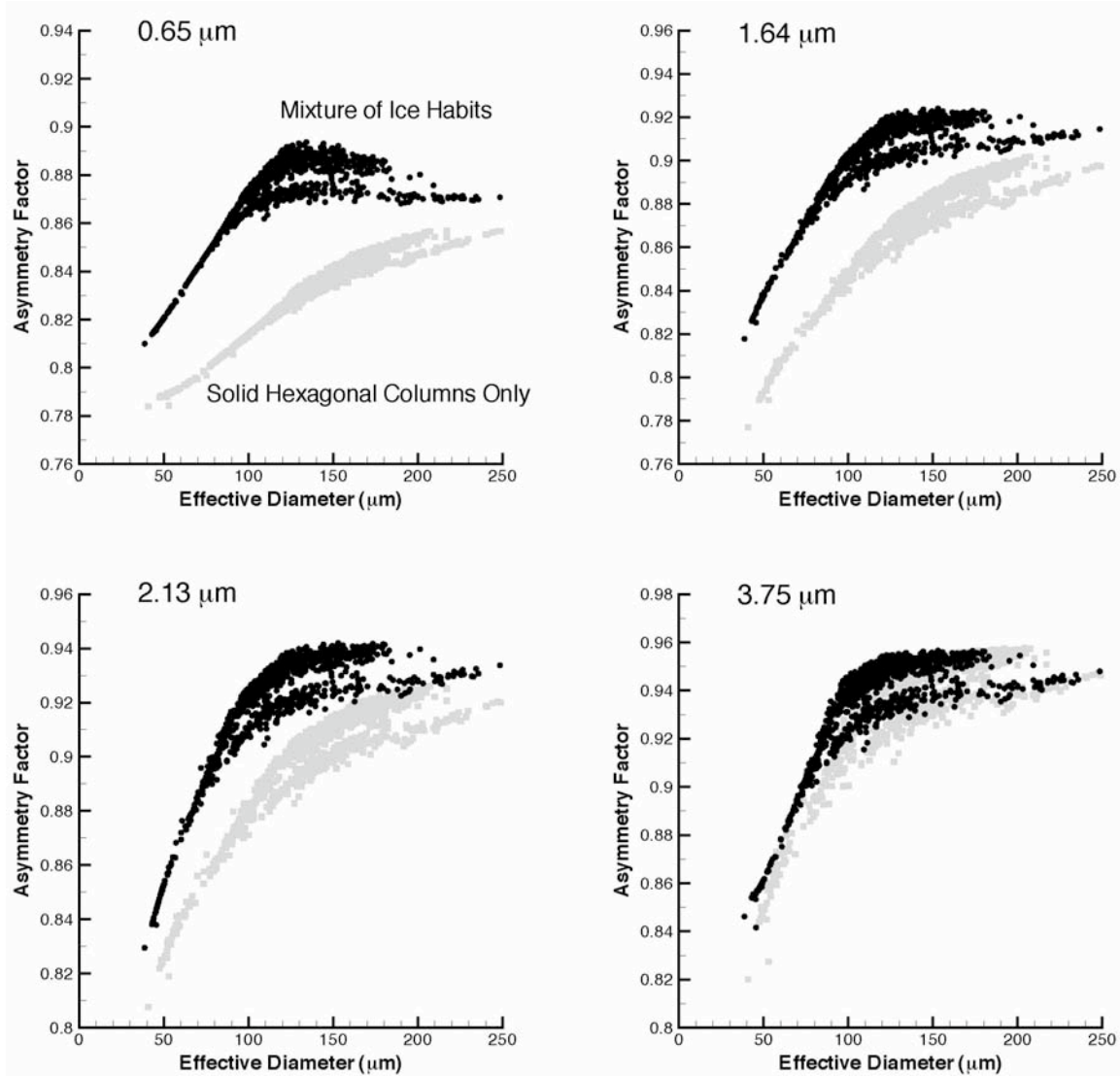
Figure 2. MODIS band-averaged single-scatter albedo calculated from *in situ* particle size distributions (PSDs) assuming a mixture of ice particle habits (black symbols), including droxtals, solid and hollow columns, plates, 3-D bullet rosettes and aggregates. Also shown are the results using the assumption of solid hexagonal columns only (gray symbols).
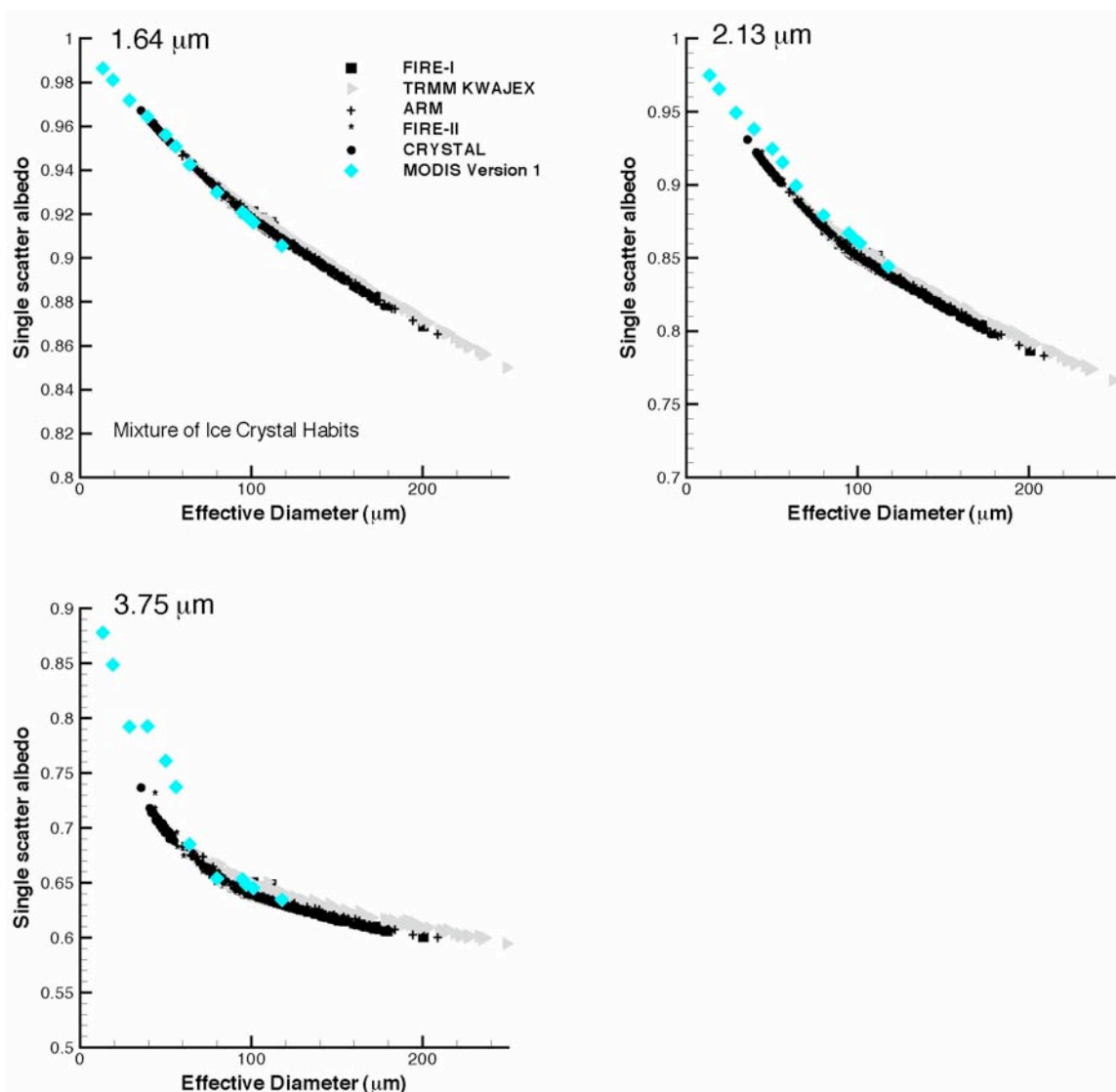
Figure 3. MODIS band-averaged asymmetry factor calculated from *in situ* particle size distributions (PSDs) assuming a single ice particle habit of solid hexagonal columns. The PSD results from FIRE-I, FIRE-II, ARM, and CRYSTAL-FACE are black symbols; the results from the TRMM KWAJEX PSD data are denoted by gray symbols.
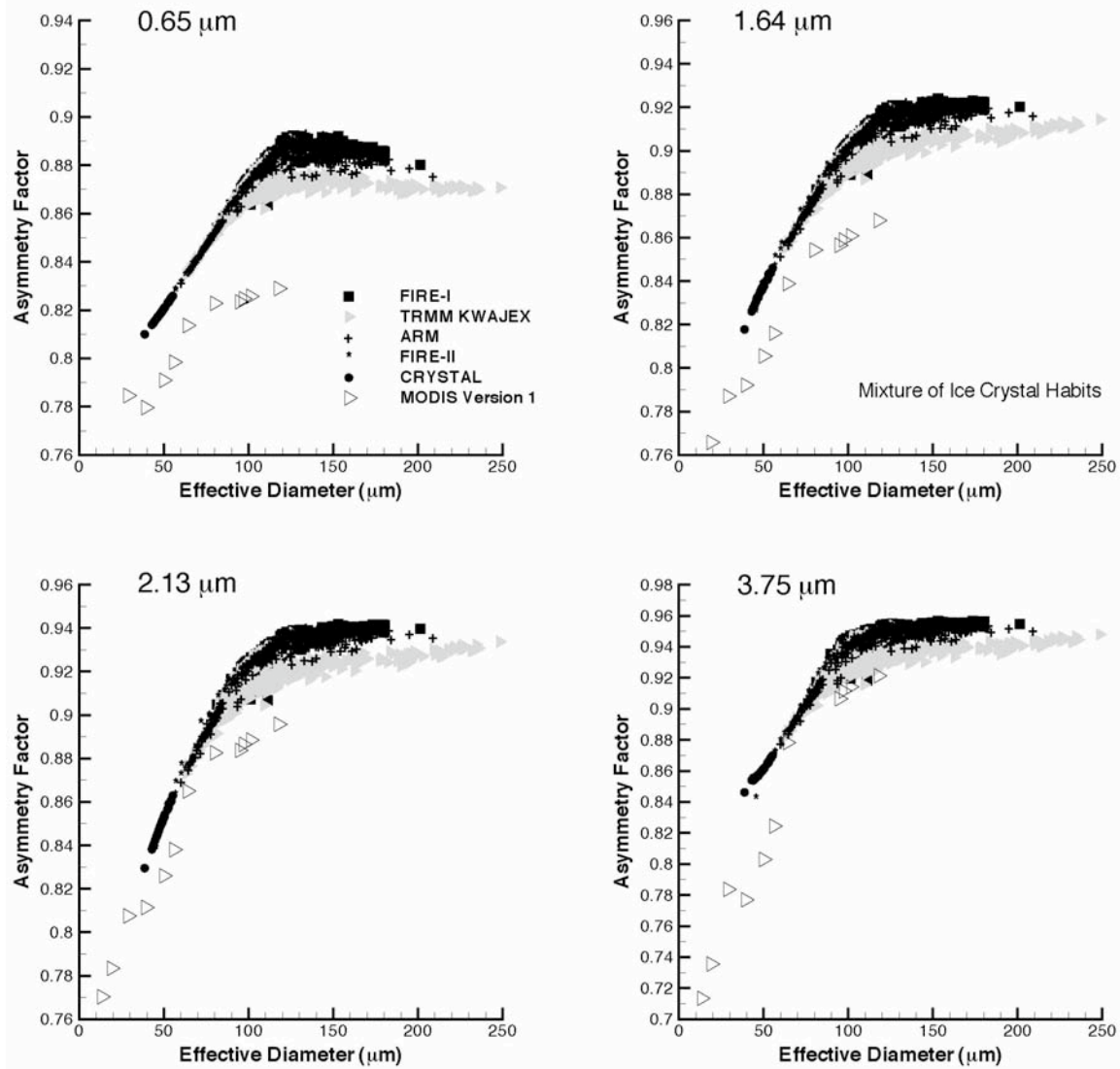
Figure 4. MODIS band-averaged asymmetry factor calculated from *in situ* particle size distributions (PSDs) assuming a mixture of ice particle habits (black symbols), including droxtals, solid and hollow columns, plates, 3-D bullet rosettes and aggregates. Also shown are the results using the assumption of solid hexagonal columns only (gray symbols).

Figure 5. MODIS band-averaged single-scatter albedo calculated from *in situ* particle size distributions (PSDs) assuming a mixture of ice particle habits. The PSD results from FIRE-I, FIRE-II, ARM, and CRYSTAL-FACE are black symbols; the results from the TRMM KWAJEX PSD data are denoted by gray symbols. Superimposed on the data are the MODIS Version 1 (V1) models.
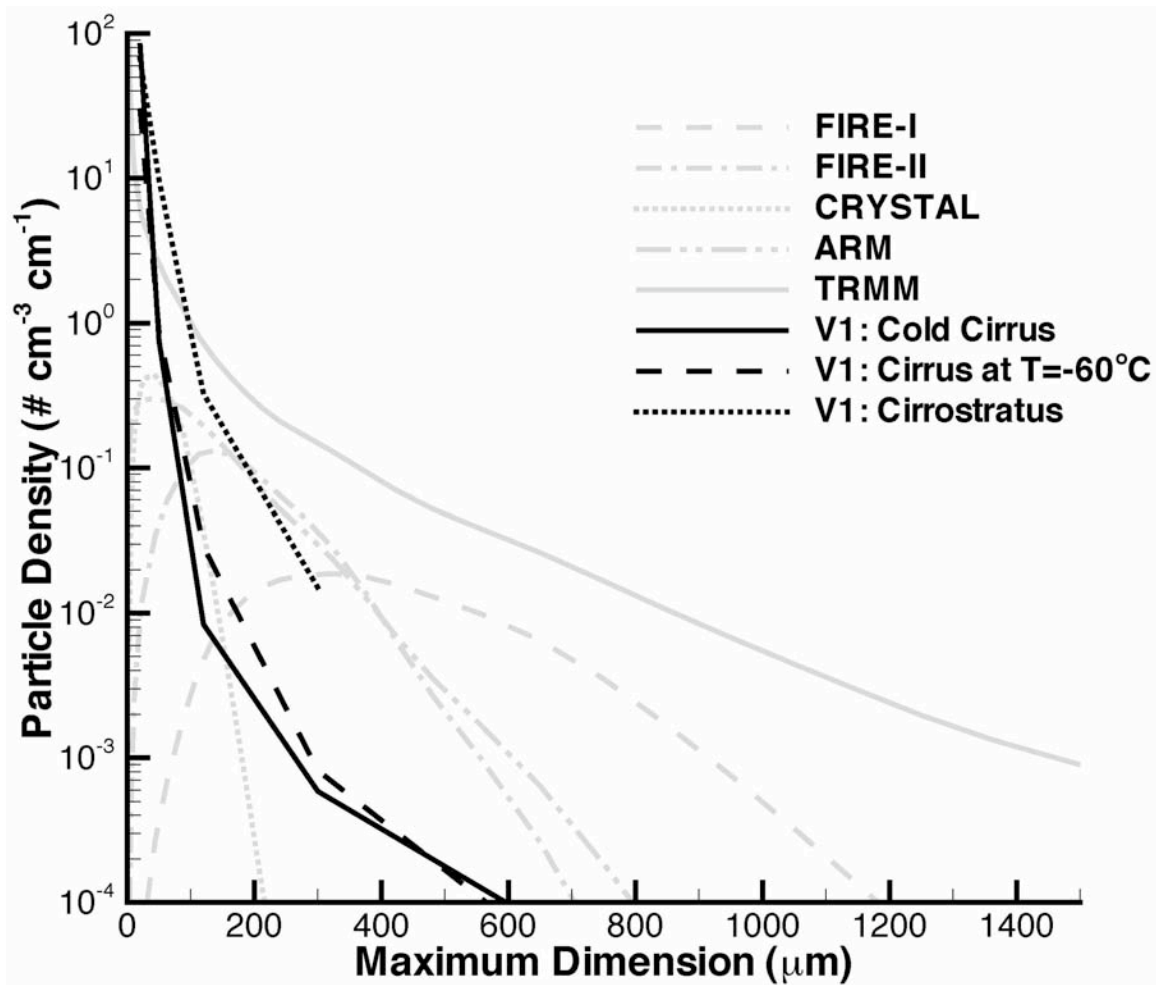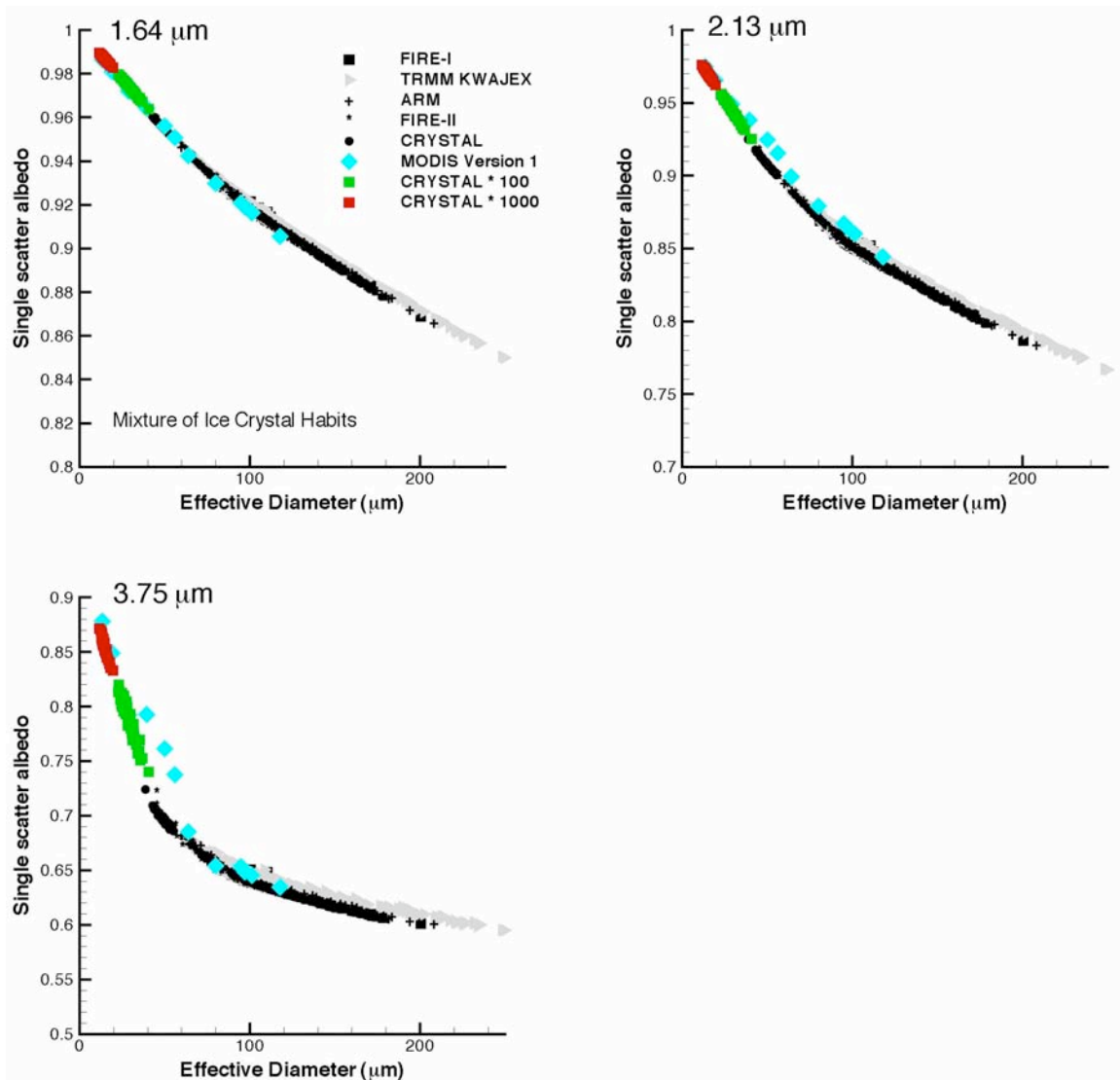
Figure 6. MODIS band-averaged asymmetry factor calculated from *in situ* particle size distributions (PSDs) assuming a mixture of ice particle habits. The PSD results from FIRE-I, FIRE-II, ARM, and CRYSTAL-FACE are black symbols; the results from the TRMM KWAJEX PSD data are denoted by gray symbols. Superimposed on the data are the MODIS Version 1 (V1) models.

Figure 7. As shown in Figure 1 in Part 1, five particle size distributions (gray lines) selected from the various field experiments. Superimposed over these PSDs are three PSDs from the MODIS Version 1 microphysical models used to generate the scattering models. These V1 models were chosen because they have the smallest effective diameters. The V1 models have at least one order of magnitude more small particles at 20 μm than at 50 μm.

Figure 8. MODIS band-averaged single-scatter albedo calculated from *in situ* particle size distributions (PSDs) assuming a mixture of ice particle habits. The PSD results from FIRE-I, FIRE-II, ARM, and CRYSTAL-FACE are black symbols; the results from the TRMM KWAJEX PSD data are denoted by gray symbols. Superimposed on the data are the results from a sensitivity study involving the CRYSTAL-FACE PSDs in which the number of particles with sizes less than 20 μm were multiplied by a factor of 100 (green symbols) or multiplied by a factor of 1000 (red symbols). The twelve MODIS V1 models are superimposed for reference (blue symbols).
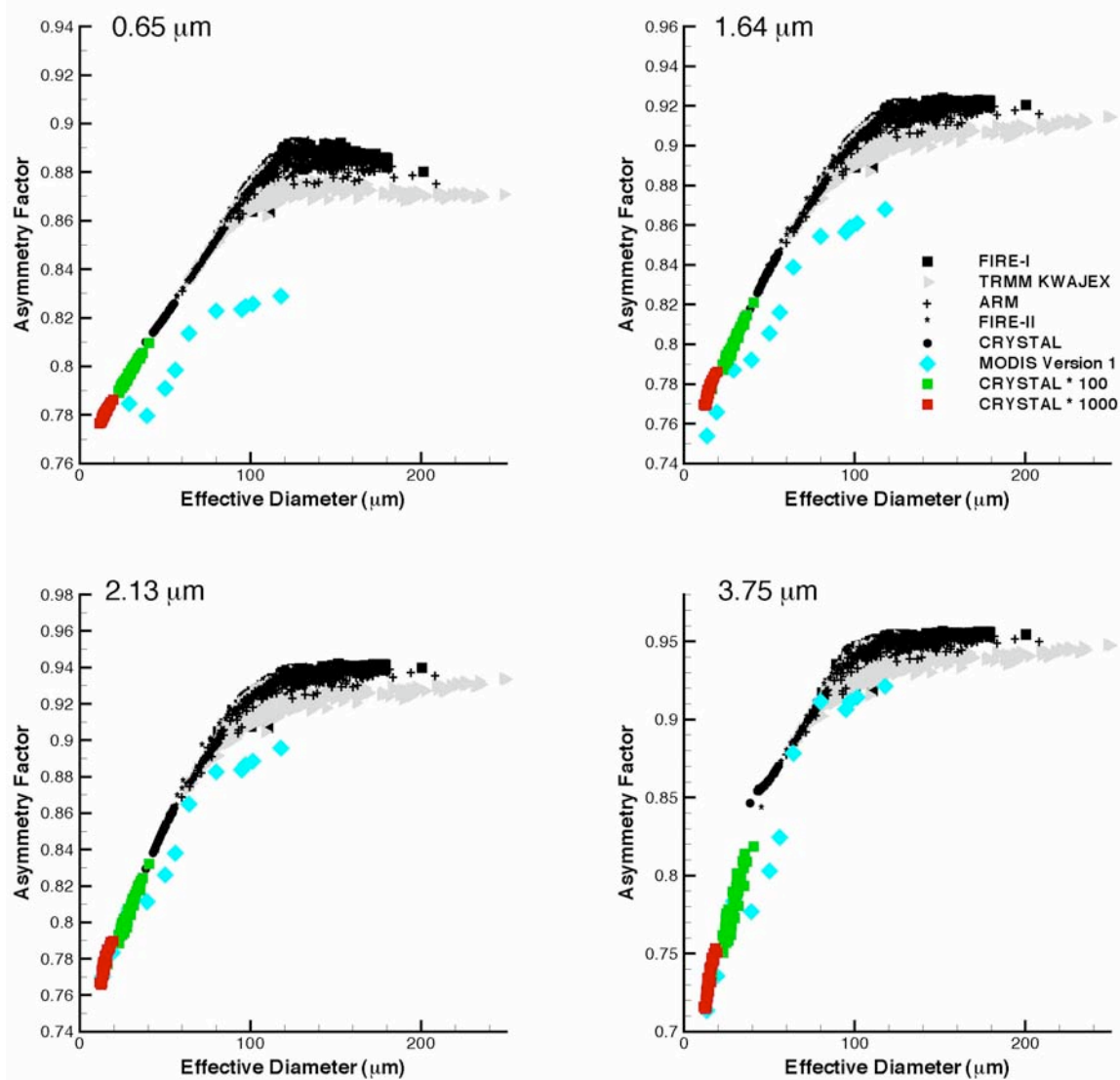
Figure 9. Same as for Figure 8 but for MODIS band-averaged asymmetry factor.
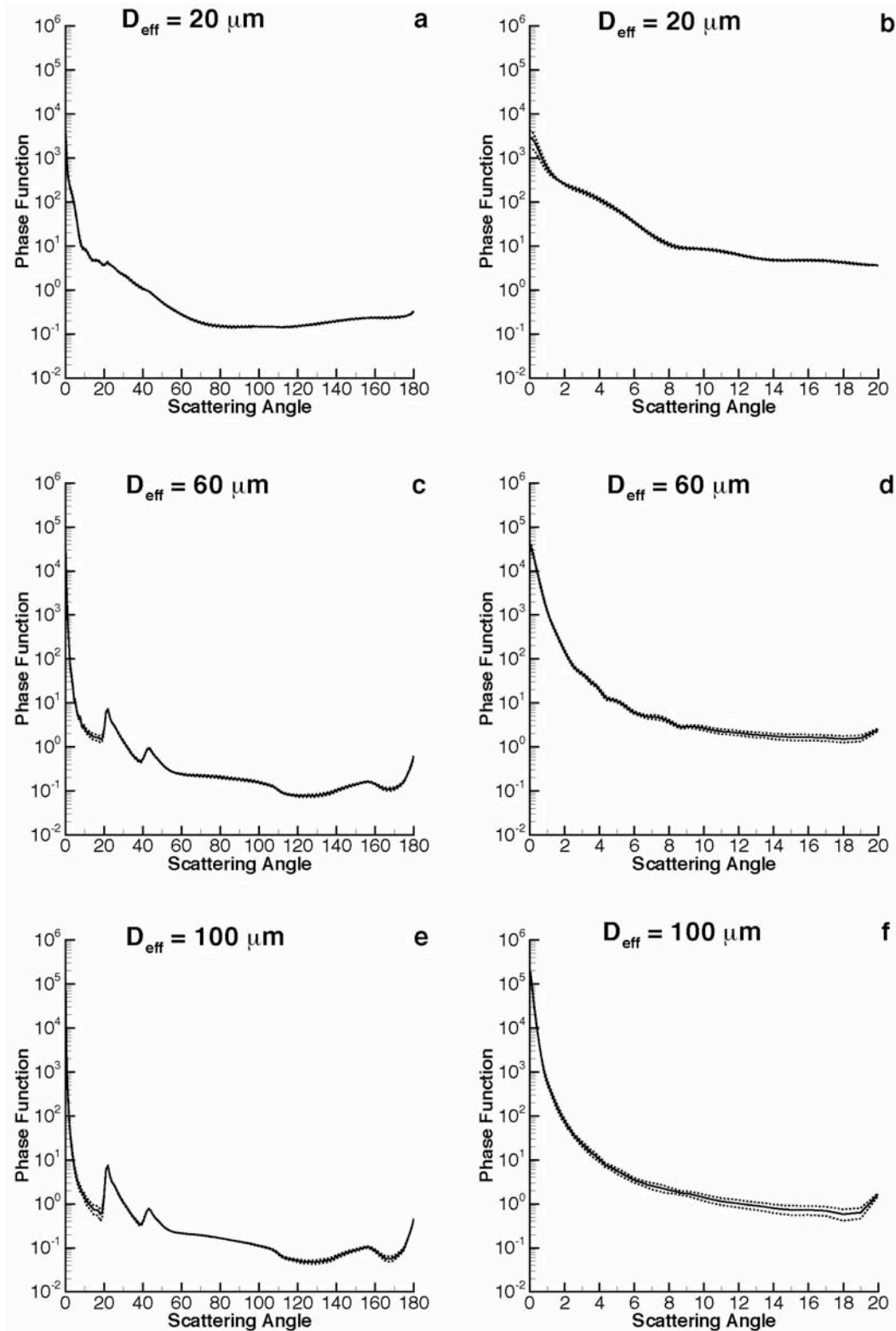
Figure 10. For MODIS band 6 (1.64 μm), the scattering phase function mean (solid line) and standard deviation (dotted line) for D_{eff} values of 20, 60, and 100 μm. The full phase function is shown in the left hand column, while the forward peak in the phase function is shown in the right hand column.

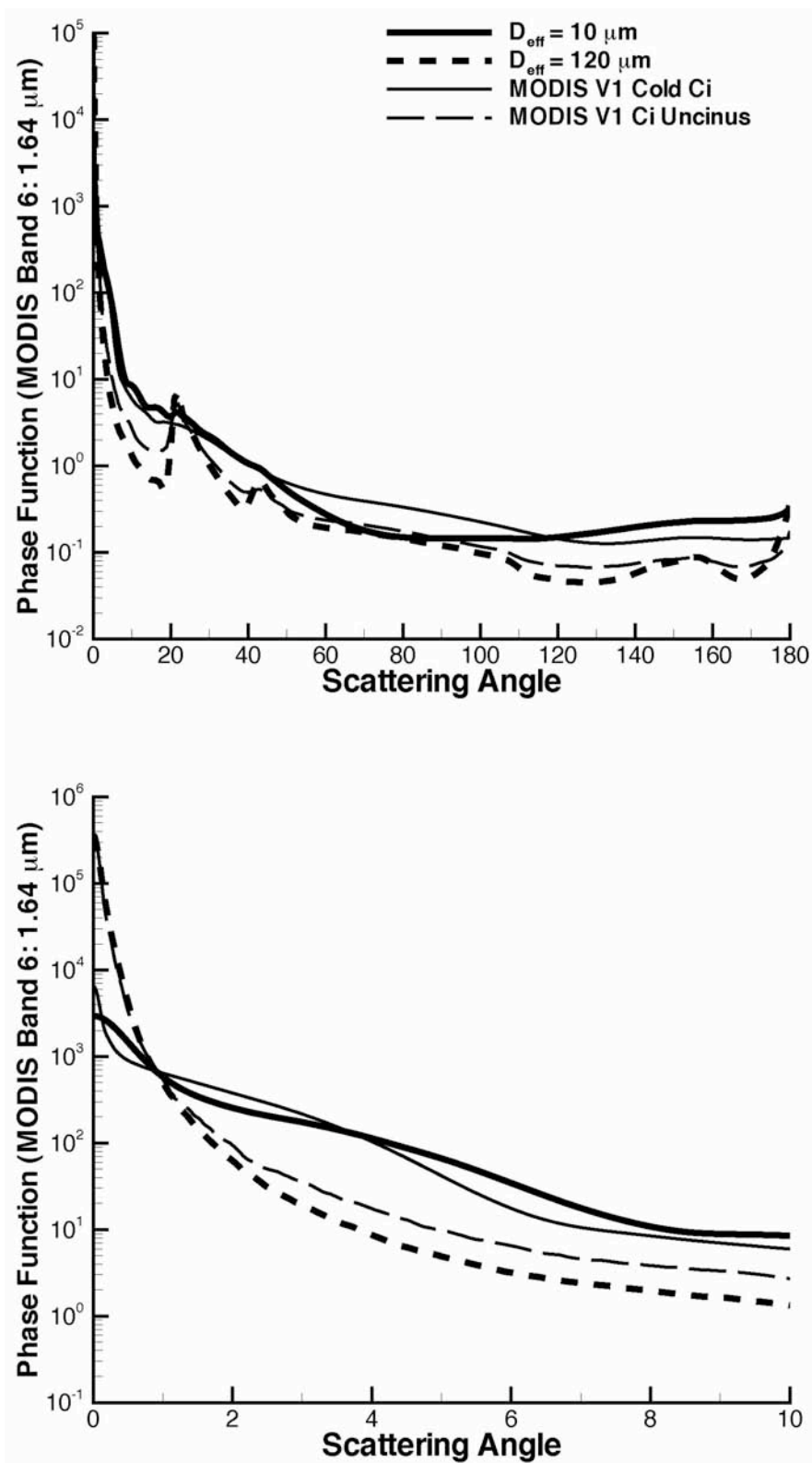Figure 11. For MODIS band 6 (1.64 μm), comparison of two MODIS V1 models (Cold Ci, D_{eff} = 13.4 μm and Ci Uncinus, D_{eff} = 117.8 μm) with two new models at D_{eff} = 10 and 100 μm.